MECHANOCHEMICAL SYNTHESIS AND SOLID-STATE CHARACTERIZATION OF MOLECULAR SALTS OF PYRIDOXINE: VIBRATIONAL SPECTROSCOPIC AND THERMAL CONSIDERATION[1]

Aleksandar Cvetkovski[1*], Ljupcho Pejov[2,3,4], Monika Stojanovska Pecova[5], Gjorgji Petrushevski[6], Petre Makreski[2]

[1]*Faculty of Medical Sciences, Goce Delcev University, 2000 Štip, North Macedonia*
[2]*Institute of Chemistry, Faculty of Natural Sciences and Mathematics, Ss. Cyril and Methodius University in Skopje, Skopje, North Macedonia*
[3]*Department of Chemistry, Bioscience and Environmental Engineering,*
Faculty of Science and Technology, University of Stavanger, 4021 Stavanger, Norway
[4]*The Polytechnic School, Ira A. Fulton Schools of Engineering, Arizona State University, AZ, USA*
[5]*Research and Development, Alkaloid AD, Blvd. Aleksandar Makedonski 12, Skopje, North Macedonia*
[6]*Quality Control Department, Alkaloid AD, Blvd. Aleksandar Makedonski 12, Skopje, North Macedonia*

aleksandar.cvetkovski@ugd.edu.mk

Crystal engineering of multicomponent crystals offers opportunities for both generic active pharmaceutical ingredients (APIs) and innovative APIs (under patent protection) to be noncovalently bound with a wide range of organic compounds, forming new solid phases such as salts or cocrystals. These multicomponent crystals can enhance the physicochemical properties, processibility, and bioavailability of the APIs. The purpose of this research is to correlate vibrational (FTIR and Raman) spectroscopy studies with the thermal behavior of new molecular salts of the drug model pyridoxine (PN), using salt formers from the group of hydroxybenzoic acid derivatives known for their potent antioxidant activity. The coformers include syringic acid (SA) and ferulic acid (FA), synthesized through eco-friendly mechanochemical methods by treating bulk powders of their stoichiometric mixture with PN. The assigned vibrational modes and thermal behaviors of the pyridoxonium syringate (PN/SA) and pyridoxonium ferulate (PN/FA·H_2O) reveal the protonation of the pyridoxine N-atom in both salts structures. This protonation results in structural alterations in the crystal packing of the counterions, which exhibit unique spectral fingerprints and thermal profiles compared to the starting compounds.

Keywords: Pyridoxine; molecular salts; spectroscopy; solid-state properties

МЕХАНОХЕМИСКА СИНТЕЗА И КАРАКТЕРИЗАЦИЈА НА МОЛЕКУЛСКИ СОЛИ НА ПИРИДОКСИН ВО ЦВРСТА СОСТОЈБА: ВИБРАЦИСКО-СПЕКТРОСКОПСКИ И ТЕРМИЧКИ СОГЛЕДУВАЊА

Кристалниот инженеринг на мултикомпонентните кристали отвора можност генеричките активни фармацевтски соединенија (API), но и иновативните API (патентно заштитени), нековалентно да се поврзуваат со широк спектар на органски соединенија, образувајќи нови цврсти фази како што се соли или кокристали. Овие мултикомпонентни кристали можат да ги подобрат физикохемиските својства, способноста за процесирање, како и биорасположливоста на самото API. Целта на ова истражување беше да се корелираат резултатите од вибрациската (инфрацрвена и раманска) спектроскопија со оние добиени од термичкото однесување на нови молекулски соли на пиридоксин (PN) користен како моделен лек. Како коформери беа користени

---

[1] Dedicated on the occasion of the Golden Jubilee of the *Macedonian Journal of Chemistry and Chemical Engineering*

соли на сирингинска киселина (SA) и ферулинска киселина (FA), кои се деривати на хидрок-сибензоеска киселина, а се познати по својата моќна антиоксидантна активност. Кокристалите беа синтетизирани со еколошки механохемиски методи преку третман на прашок од секој коформер со PN во стехиометриски однос. Асигнираните вибрациски модови и термичкото однесување на добиените продукти, пиридоксониум сирингат (PN/SA) и пиридоксониум ферулат (PN/FA·H₂O), го потврдија протонирањето на N-атомот на пиридоксин во структурата на двете соли. Ова протонирање внесува структурна промена на кристалното пакување на контра-јоните, што доведува до различни спектри и термички профили во споредба со оние на почетните соединенија.

Клучни зборови: пиридоксин; молекулски соли; спектроскопија; својства на цврста состојба

1. INTRODUCTION

For marketing authorization, regulatory authorities have approved 9 out of 10 new active pharmaceutical ingredients (APIs) as solid phases.[1] Moreover, among all new drug candidates in development pipelines, 60 % possess high molecular weight and lipophilic structures, which compromise their bioavailability. Among pharmaceutical formulations, 65–70 % of the market share belongs to solid dosage forms, with 50 % of these comprising the salt forms of APIs.[2]

However, the concept of rational API salification remains constrained by decision-tree processes that prioritize empirical matching of pKa values with a limited range of soluble atomic or molecular counterions. These counterions must effectively deprotonate acidic drugs or protonate basic drugs in solutions with specific solvent polarities.[3–10] Despite achieving solubility in solution, isolating such salts as solid multicomponent phases with cocrystallized cations and anions is not always feasible.[11–13]

Additionally, for toxicological compliance in pharmaceutical salts, the selection of acidic or basic salt formers extends to the GRAS (Generally Recognized as Safe) list of FDA-approved food additives. These additives can act as coformers in cocrystallization with various APIs, facilitating neutral, noncovalent interactions through hydrogen bonding rather than ionized interactions.[14–18] Consequently, the design of multicomponent solids relies on crystal engineering principles, where noncovalent molecular recognition drives the bottom-up building of supramolecular structures into single-phase multicomponent crystals.[19,20]

This approach allows tailored design of crystals to modulate the properties of APIs, such as solid-state form, hygroscopicity, particle size and shape, flowability, solubility, and pharmacokinetic profile. These properties differ significantly when APIs are transformed into crystallized multicomponent phases with selected coformers. The smallest spatial motifs of noncovalent interactions, known as synthons, connect API and conformer molecules in stoichiometric ratios. These synthons are directional and repeatable patterns extending throughout the long range crystal lattice, defining the structures of multicomponent crystals.[21–23]

Regulatory authorities use the degree of proton transfer in noncovalent interactions as a benchmark for defining pharmaceutical salts and cocrystals. Salts are characterized by a complete charge transfer between cocrystallized ion pairs, while cocrystals involve neutral APIs and conformers formed through non-ionic interactions.[24–26] However, the variety of molecular and crystal structures of APIs and coformers enables a continuum of multicomponent crystal forms, including salt cocrystals, ionic cocrystals, or zwitterionic cocrystals.[27,28]

Many coformers from natural or botanical sources, which are included in the GRAS list and used in nutraceuticals or food-supplements, exhibit biological activity, such as antioxidative properties. These coformers can cocrystallize with APIs, enhancing the thermodynamic and chemical stability of the native API and modulating its therapeutical effects while maintaining dose regimen safety.[29–31]

Contributing to the growing trend of cocrystallizing APIs with natural-source coformers, we report a mechanochemical method for the large-scale preparation and solid-state characterization of two molecular salts of pyridoxine: pyridoxonium syringate and pyridoxonium ferulate. The crystal structures of these compounds were previously resolved during screening involving derivatives of hydroxybenzoic acid.[32–34]

Pyridoxine (PN), widely known as vitamin B6, is commonly used in mono- or combination therapies and is commercially available only as the hydrochloride salt of its protonated pyridoxonium cation. In this study, pyridoxine served as the model API for exploring cocrystallization with syringic acid and ferulic acid.

PN is a water-soluble compound and one of three structural analogs, along with pyridoxal (PL)

and pyridoxamine (PM), all of which are converted in the body to the active form, pyridoxal 5-phosphate (P5P). The electron-withdrawing molecular structure of P5P destabilizes the alpha-carbon atom, enabling its role as a coenzyme in reactions such as transamination, decarboxylation, and elimination in amino acid, protein, carbohydrate, and lipid metabolism, as well as in neurotransmitter synthesis.[35,36]

Hydrochloride salts, including pyridoxine hydrochloride, offer many advantages, such as increased gastric absorption,[37] enhanced water solubility of protonated weak bases,[5] improved salt-excipient compatibility, and low-cost production using hydrochloric acid as a counterion.[38] However, they also present several drawbacks, including corrosiveness during powder processing,[38] high hygroscopicity, and a tendency for disproportionation.[39] This is accompanied by volatility and drug precipitation under acidic pH conditions due to the common-ion effect.[5,40] Additionally, polymorphic diversity[41] and alternated pharmacokinetic profiles[37] complicate the development of hydrochloride salts.

To address these challenges, there is growing interest in the holistic approach to developing molecular salts of a pyridoxine-free base with counterions from natural organic acids that also possess therapeutic properties, potentially adding value to pyridoxine use. For example, syringic acid (SA) and ferulic acid (FA) are phenolic compounds of natural origin with many therapeutic properties, including antioxidative. This activity is attributed to the stabilization of their phenolic rings through electron-donating methoxy groups.[42,43] The extended conjugation in the side chain of FA enhances its ability to quench resonance-stabilized phenoxy-free radicals, making FA an effective membrane antioxidant that scavenges free radical superoxide anions and inhibits lipid peroxidation.[44]

Beyond their antioxidant activities, SA and FA demonstrate therapeutic potential through their capacity to modulate the dynamics of proteins, transcriptional factors, growth factors, and signaling molecules as biological targets in diseases such as diabetes, cardiovascular diseases, cancer, cerebral ischemia, neurodegenerative disorders, and liver damage. They also exhibit antimicrobial, anti-inflammatory, and antiendotoxic effects.[43] For instance, microencapsulation of pyridoxine in FA-grafted chitosan microspheres has confirmed its anti-inflammatory activity and potential as a novel dietary supplement or a functional food ingredient.[45] Furthermore, the synergistic potential of vitamin B6 with other antioxidants is demonstrated in studies such as the influence of B6 vitamins on the antioxidant activity of catechins (polyphenols in green tea extract) using the 2,2-diphenyl-1-picrylhydrazyl (DPPH) assay.[46] This paves the way for exploring the synergistic effects between pyridoxine and syringic acid and ferulic acid.

An innovative aspect of this research is the application of an eco-friendly mechanochemical treatment to solid binary mixtures of PN with SA or FA in stoichiometric ratios. This approach enables thermomechanical activation of the surface of the solid particles, facilitating their conversion into pyridoxonium syringate (PN/SA, Fig. 1a) and pyridoxonium ferulate (PN/FA·H_2O, Fig. 1b) salts, respectively. By avoiding the use of toxic organic solvents typically used in conventional organic synthesis, this method significantly reduces environmental and health risks.
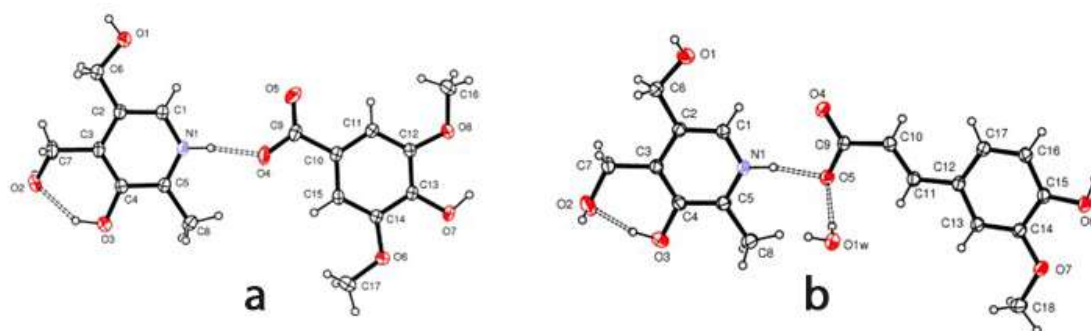

Fig. 1. ORTEP view of: (**a**) PN/SA and (**b**) PN/FA·H_2O with displacement ellipsoids drawn at the 40 % probability level. Hydrogen bonds are drawn as dashed lines.[34]

This study extends on previously determined crystallographic structures of these salts,[34] shifting the focus to a sustainable synthesis approach and its potential benefits. Furthermore, the authenticity of these salts was rigorously confirmed through X-ray powder diffraction, with the results meti-

culously correlated to structures derived from single-crystal growth. Beyond structural characterization, the study provides a comprehensive analysis integrating experimental vibrational spectroscopy with theoretical simulations, shedding light on the unique intermolecular interactions in these salts.

Finally, detailed thermal profiling was performed to evaluate their stability and decomposition behavior, advancing our understanding of their physicochemical properties and further highlighting the uniqueness of this research.

2. EXPERIMENTAL SECTION

2.1. *Material and methods*

The pyridoxine-free base (PN) was isolated by treating an aqueous solution of PN hydrochloride with an equimolar amount of $NaHCO_3$, followed by a two-step liquid-liquid extraction using methylene chloride. The methylene chloride extract was dried over anhydrous $MgSO_4$ before roto-evaporation of the solvent, yielding a white solid phase confirmed as pyridoxine-free base. SA, FA, and all other substances were commercially available (Sigma-Aldrich) and used without further purification. Solvents of analytical or chromatographic grade were obtained from a local supplier (Alkaloid AD).

2.2. *Mechanochemical synthesis of pharmaceutical salts: pyridoxonium syringate (PN/SA) and pyridoxonium ferulate monohydrate (PN/FA·H₂O)*

Manual mechanochemical grinding was performed separately for two mixtures: Mixture **1** – PN and SA in a 1:1 stoichiometric ratio of PN (44.3 mg, 0.1 mmol) and SA (52 mg, 0.1 mmol); and Mixture **2** – PN and FA in a 1:1 stoichiometric ratio of PN (66.21 mg, 0.1 mmol) and FA (76 mg, 0.1 mmol). Each mixture was ground in a mortar with pestle, and a few drops of 70% v/v ethanol were added to convert the powders into pastes during a kneading process that lasted 15 min. The resulting solid mixtures were then left to dry overnight in a desiccator.

2.3. *X-ray powder diffraction*

The reproducibility of the two preparation procedures (single-crystal growth vs. bulk powder synthesis) was optimized by comparing the calculated diffractograms of single crystals[47] with the X-ray powder diffraction (XRPD) patterns of the mechanochemically synthesized PN/SA and PN/FA·H₂O samples.

X-ray powder diffraction measurements were carried using a Rigaku Ultima IV diffractometer equipped with a Cu$K\alpha$ source ($\lambda = 1.54178$ Å) generated by an X-ray tube operating at 40 kV and a current of 40 mA. The $K\beta$ filter was employed, and the following optical components were used: a 2/3° divergence slit, a 10 mm divergence height slit, and an 8 mm scattering slit. Diffraction data were collected over a 2θ range of 4º to 50º at a constant scanning rate of 4°/min, utilizing a high-speed position-sensitive linear (1D) D/teX Ultra detector.

2.4. *Vibrational spectroscopic analysis*

The Varian-660 Fourier transform infrared (FTIR) spectrometer was used to acquire the FTIR spectra. Attenuated total reflectance (ATR) spectra were collected at a resolution 4 cm^{-1}, with 16 scans per spectrum at room temperature and 5 scans per spectrum for temperature-resolved measurements. The GladiATR module with a diamond crystal (PIKE Technologies) was used for these analyses.

Raman spectra at room temperature (20 °C) were recorded using a Horiba JobinYvon LabRam 300 micro-Raman multichannel spectrometer. An Olympus MPlanN confocal microscope with a ×50 long-distance objective was chosen for magnification. The position on the sample surface was adjusted with a motorized *x-y* stage.

The Raman effect was obtained using the 632.8 nm line of a He:Ne laser at a power of 1.9 mW. Backscattered radiation was analyzed in a 180° configuration using an 1800 lines/mm grating monochromator. Raman intensities were collected with a thermoelectrically cooled CCD array detector. The wavenumber accuracy was ±1 cm^{-1}, calibrated using the Rayleigh line and the 520.5 cm^{-1} line of the Si standard.

FTIR and Raman spectra were recorded in the wavenumber regions of 4000 – 540 cm^{-1} and 4000 – 100 cm^{-1}, respectively.

2.5. *Thermal analysis*

Differential scanning calorimetry (DSC) measurements were performed using a Netzsch DSC 204 F1 Phoenix instrument, with samples (2 – 3 mg) placed in pierced aluminum pans, under a dynamic nitrogen atmosphere (30 ml/min). Samples were heated from room temperature to 200 °C or higher, depending on their thermal stability, at a heating rate of 10 °C/min.

Thermogravimetric (TG)/DTG analyses were performed on a Netzsch TG 209 F1 Iris thermogravimetric analyzer, with open Al_2O_3 sample pans. The

temperature range for the analyses was 25 – 300 °C or 25 – 400 °C, depending on the thermal stability of the samples, at a heating rate of 10 °C/min, under dynamic nitrogen atmosphere (30 ml/min).

2.6. *Density functional tight binding (DFTB) calculations*

In the present study, we employed the density functional tight binding (DFTB) method.[48] The choice of this methodology was dictated by the size of the studied systems. It is computationally feasible and still sufficiently accurate to derive chemically relevant conclusions concerning molecular structure and dynamics features.

As an approximation to the exact Kohn-Sham (KS) method, the DFTB method shares common features with essentially all tight binding methods. The coefficients of the Linear combination of atomic orbitals-molecular orbital (LCAO-MO) expansion are obtained by solving the KS secular-type equation:

$$\sum_v c_{vi}\left(H_{\mu v} - \varepsilon_i S_{\mu v}\right) = 0 \; ; \; \forall \mu, i \qquad (1)$$

where $S_{\mu v}$ is the overlap matrix element, and the Hamiltonian matrix elements $H_{\mu v}$ explicitly depend on the Mulliken charges. As these are dependent on the MO coefficients, equation (1) needs to be solved in a self-consistent manner. The Slater-Koster approach, implemented in this study, uses precomputed values of $H_{\mu v}$, along with tabulated values of the overlap matrix elements for different distances.

Different variants of the DFTB method have been derived from expanding the electron density $\rho(r)$ around a reference density $\rho_0(r)$ in a perturbation-like manner:

$$\rho(r) = \rho_0(r) + \delta\rho(r) \qquad (2)$$

From equation (2), one can derive the Taylor expansion of the energy functional:

$$E[\rho(r)] = E[\rho_0(r)] + \int \left(\frac{\delta E[\rho(r)]}{\delta\rho(r)}\right)_{\rho_0} \delta\rho(r) +$$
$$\frac{1}{2}\iint \left(\frac{\delta^2 E[\rho(r)]}{\delta\rho(r)\delta\rho(r\prime)}\right)_{\rho_0} \delta\rho(r)\delta\rho(r') + \dots \qquad (3)$$

In this study, we employed the *third order* DFTB method (DFTB3), which expands the total electronic energy in a Taylor series up to the *third order* with respect to charge fluctuations:[49]

$$E_{\text{DFTB3}} = \sum_i n_i \sum_{\mu v} c_{\mu i} c_{vi} H_{\mu v}^0 +$$
$$\frac{1}{2}\sum_{ab} \Delta q_a \Delta q_b \gamma_{ab} + \frac{1}{3}\sum_{ab} \Delta q_a^2 \Delta q_b \Gamma_{ab} + E^{\text{rep}} \quad (4)$$

where $c_{\mu i}$ and c_{vi} are the wavefunction expansion coefficients, $H_{\mu v}^0$ are the Hamiltonian matrix elements, and Δq_a and Δq_b, represent charge fluctuation at sites (atoms) a and b, respectively. E^{rep} is the short-range repulsive energy term. The term Γ_{ab} is the derivative:

$$\Gamma_{ab} = \left(\frac{\partial\gamma_{ab}}{\partial q_a}\right)_{q_a^0} = \left(\frac{\partial\gamma_{ab}}{\partial U_a}\frac{\partial U_a}{\partial q_a}\right)_{q_a^0}, \; a \neq b \quad (5)$$

The function γ_{ab} represents the Coulomb repulsion between the density fluctuations (considering spherically constrained atomic densities) and is given by:

$$\gamma_{ab} = \frac{1}{r_{ab}} - S(r_{ab}, U_a, U_b) \cdot h(r_{ab}, U_a, U_b)\dots(6)$$

where S is a short-range function introduced to ensure the correct convergence behavior of γ as $r_{ab} \to 0$, while h is a damping function. The parameters U_a and U_b denote the corresponding Hubbard parameters for atoms a and b, respectively.

The DFTB+ code[50] was used for all DFTB computations in the present study. The 3ob Slater-Koster parameter set for bio- and organic molecules was used throughout the calculations.[51–53] Optimization of the atomic positions in the unit cell of the investigated 3D periodic system was conducted using a rational function-based optimization algorithm. After carefully testing (controlling) the convergence of energy, which was better than 10^{-4} eV, as well as the convergence of the geometry parameters, the productive calculations were performed with the Γ-point-centered 8 × 8 × 8 Monkhorst-Pack k-point grids' sampling. Charge self-consistent (SCC) tolerance was set to 10^{-8} a.u. during geometry optimizations and at 10^{-8} a.u. for Hessian computations.[54]

3. RESULTS AND DISCUSION

3.1. *Authentication of the mechanically synthesized salts by XRPD with single crystals of the corresponding compounds*

The calculated X-ray patterns of PN/SA and PN/FA·H₂O, obtained from single crystals,[47] were compared with the experimental patterns of solid samples prepared by mechanochemistry. The XRPD pattern of the sample obtained from mixture **1** corresponded to the theoretical XRD pattern generated from the CIF of pyridoxonium syringate, PN/SA (Figure 1S). In contrast, mechanosynthesis of mixture **2** resulted in cocrystallization into a salt whose structural identity corresponded to pyridoxonium ferulate monohydrate (PN/FA·H₂O, Fig. 2S).

3.2. *IR/Raman spectra*

3.2.1. *Deprotonated pyridoxine (neutral base), PN*

Characteristic vibrational bands in the FTIR spectra of deprotonated PN (neutral base as a drug model), the conformers SA and FA, and their cor-responding salts (where the pyridoxonium cation is protonated) are shown in Figures 2 and 3, respectively. The Raman spectra of these compounds are presented in Figure 4, while the characteristic bands in the FTIR and Raman spectra of all compounds are given in Tables 1S and 2S.
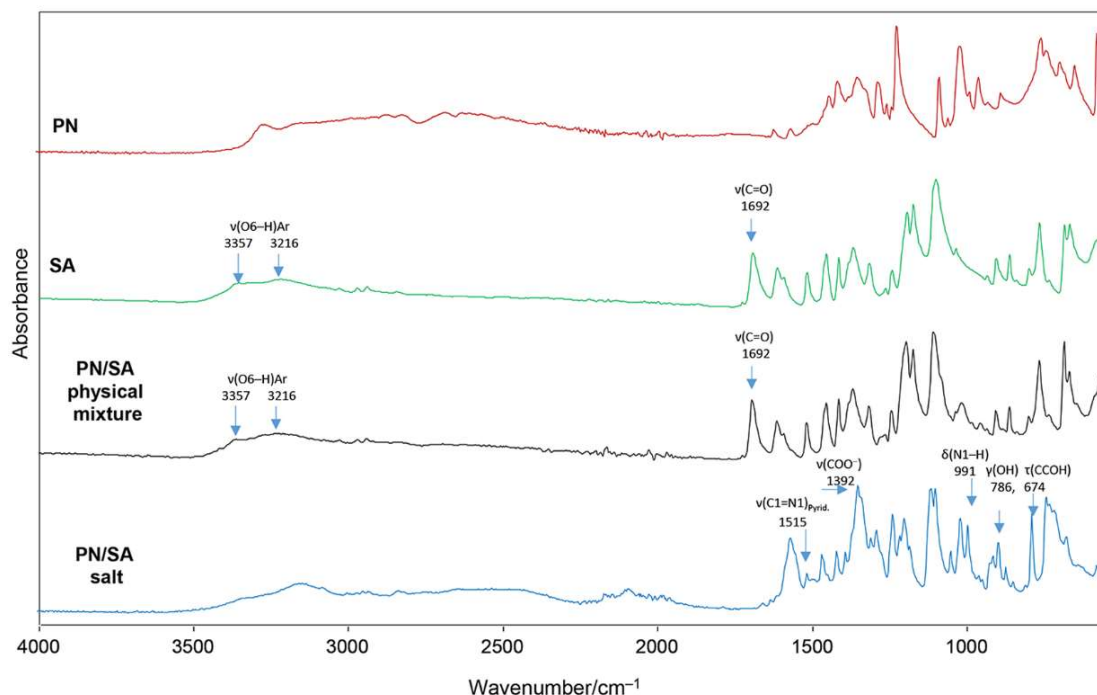

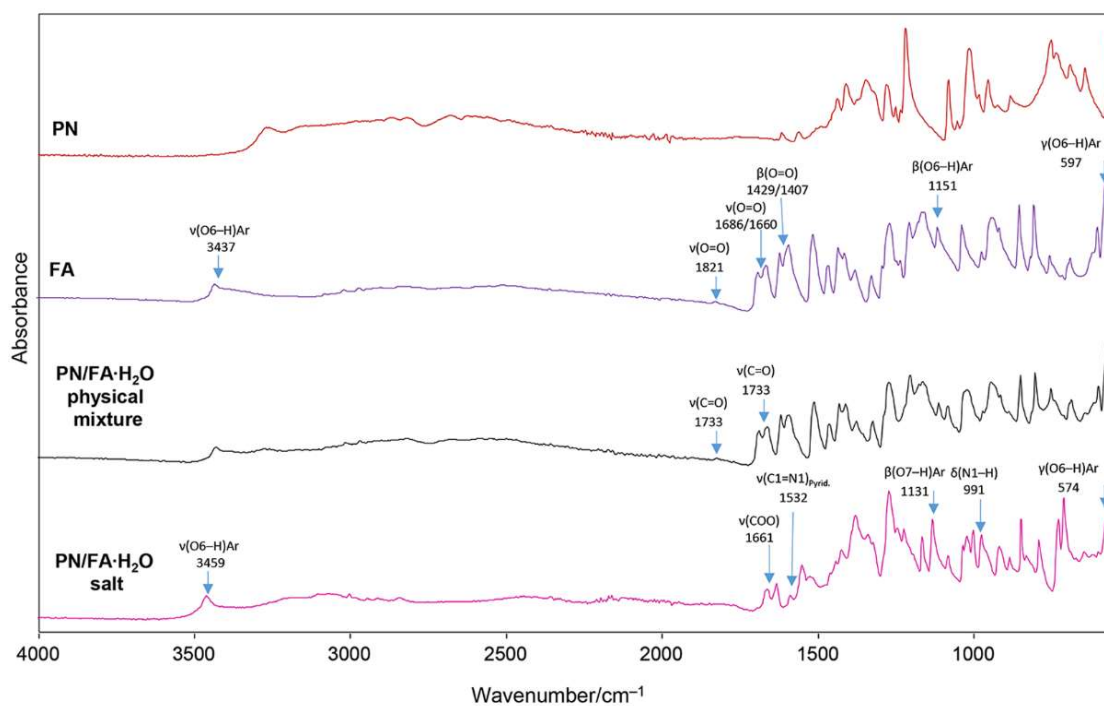**Fig. 2.** FTIR spectra of PN, SA, PN/SA (physical mixture), and PN/SA (salt)

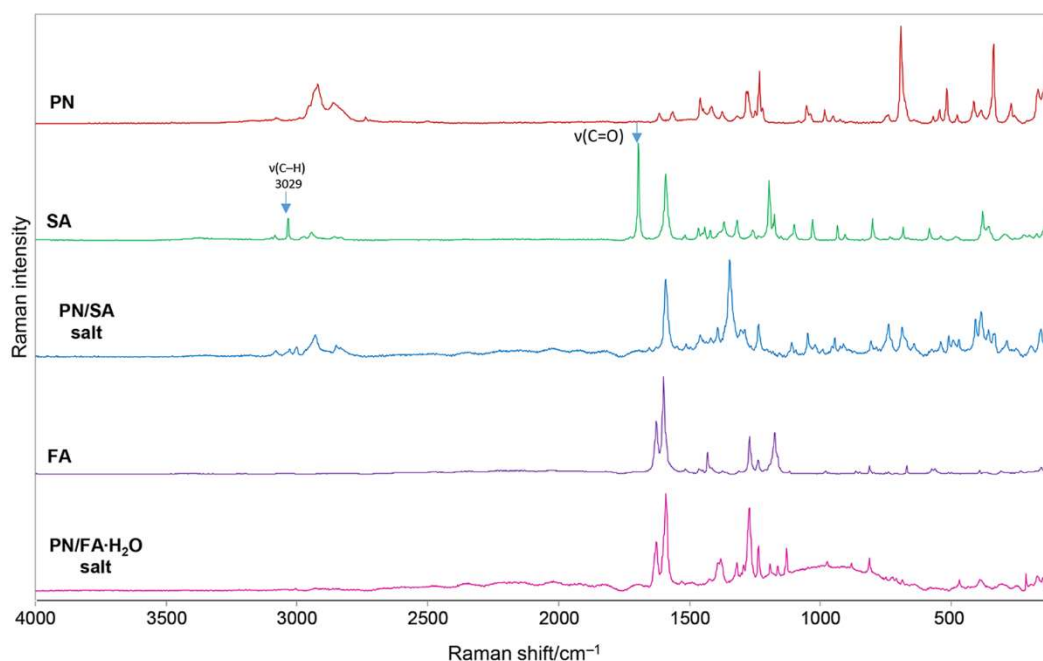**Fig. 3.** FTIR spectra of PN, FA, PN/FA (physical mixture), and PN/FA·H₂O (salt)

Fig. 4. Raman spectra of PN, SA, PN/SA salt, FA, and PN/FA·H₂O salt

3.2.1.1. *CH₃ group vibrational modes*

The CH stretching vibrations occur in the $3100 - 3000$ cm^{-1} range for aromatic structures, with bands in this region attributed to pure and highly localized modes that remain unaffected by the nature of the substituents.[55] Asymmetric and symmetric CH₃ stretching modes are assigned in the $2992 - 2818$ cm^{-1} region in the FTIR and Raman spectra of PN, PN/SA, and PN/FA·H₂O salts. Additionally, bending modes are observed around 1460 cm^{-1} (Tables 1S and 2S).

Our DFTB calculations predict a series of bands for methyl group stretching modes with centroids at 2987 cm^{-1}, 2873 cm^{-1}, and 2850 cm^{-1}. The corresponding bending modes are predicted to appear at 1523 cm^{-1} and 1487 cm^{-1}.

3.2.1.2. *C–H group bands*

The CH stretching bands for pyridine are observed in the $3095 - 3030$ cm^{-1} range.[56] In-plane and out-of-plane bending vibrations, evidenced at 1459/1448 cm^{-1} (Raman) and 884 cm^{-1} (FTIR) for PN[57,58] are shifted to higher wavenumbers in the spectra for PN/SA and PN/FA·H₂O salts (Tables 1S and 2S). The planar C–H bending vibrations are observed in the $1350 - 950$ cm^{-1} region.[58]

DFTB predictions align with these empirical assignments, with the C–H stretching band centroid predicted at 3072 cm^{-1}, the in-plane bending at 1465 cm^{-1}, and the out-of-plane bending mode at 834 cm^{-1}.

3.2.1.3. *Pyridine ring bands*

The pyridine ring exhibits six stretching modes: five in the $1650 - 1200$ cm^{-1} region, which are affected by the molecular structure of the substituents to the ring, and one in the $1100 - 600$ cm^{-1} region, known as ring breathing, which is also influenced by the substituents.[59] In the Raman spectrum (Fig. 4, Table 2S), stretching vibrational modes of the PN ring [ν(C3–C4), ν(C2–C3), and ν(C4–C5)] are observed at 1620 cm^{-1}, 1560 cm^{-1}, and 1040 cm^{-1}, respectively.

Out-of-plane ring deformations are assigned at 749/741 cm^{-1} and 544 cm^{-1} in the Raman spectrum of PN (Table 2S), while an in-plane ring deformation band appears at 478 cm^{-1}. In the FTIR spectrum of PN, these bands appear are observed in the $926 - 573$ cm^{-1} range (Table 1S). However, these modes are not clearly evident in the spectra of PN/SA and PN/FA·H₂O due to coupling interference with other modes arising from the coformer structural units.

Two stretching vibrations, ν(C2–C6) and ν(C3–C7), produce Raman bands at 1020 cm^{-1} and 924 cm^{-1}, respectively, while two medium-to-strong deformation modes, γ(C3–C7) and τ(C5–C8), appear at 273 cm^{-1} and 113 cm^{-1} for PN, respectively (Table 2S).

Our DFTB calculations align well with these empirical assignments. The C–C stretching modes within the pyridine ring are predicted to result in bands with centroids at 1645 cm^{-1}, 1585 cm^{-1}, 1045

cm^{-1}, 978 cm^{-1}, and 900 cm^{-1}, followed by in-plane deformations at 823 cm^{-1} and 734 cm^{-1} and out-of-plane deformations at 432 cm^{-1} and 328 cm^{-1}.

3.2.1.4. *CH₂ bands*

The deformation bands for the modes δ(C6–H), δ(C7–H), and δ(C6–H) are observed at 1083 cm^{-1}, 1052 cm^{-1}, and 955 cm^{-1} in the PN FTIR spectrum, respectively (Table 1S).

The corresponding DFTB predictions are 1105 cm^{-1}, 1097 cm^{-1}, and 1044 cm^{-1}, respectively.

3.2.1.5. *C–OH bands*

The C4–OH group vibration in the pyridine ring is characterized by its bending vibrations, β(C4–O3) and γ(C4–O3), observed at 517 cm^{-1} and 571 cm^{-1}, respectively, and a torsion mode, τ(C4–O3), at 692 cm^{-1} in the Raman spectrum of PN (Table 2S, Fig. 4).

The corresponding DFTB-predicted values are 623 cm^{-1}, 561 cm^{-1}, and 495 cm^{-1}, respectively.

3.2.2. *Syringic acid (SA) and PN/SA salt*

The absence of a center of symmetry in the studied salts contributes to their fundamental activity in both FTIR and Raman spectra (Fig. 2 and Fig. 4; Tables 1S and 2S).

Two broad bands at 3357 cm^{-1} and 3216 cm^{-1} in SA, which also appear with weak intensities in the FTIR spectrum of the PN/SA physical mixture (Fig. 2), are related to the vibrational stretching ν(O–H) in the carboxylic group (COOH) and the phenol moiety. These bands diminish in the spectrum of PN/SA salt, indicating that the carboxylic and phenol groups participate in salt formation with the PN molecule via hydrogen bonding interactions.

Additionally, weak bands at 3412 cm^{-1} and 3343 cm^{-1} in the PN/SA salt, as well as at 3216 cm^{-1} in SA (absent in the formed salt). The shifting of bands to 3007 cm^{-1} for SA, 2970 cm^{-1} for the PN/SA salt, 2938 cm^{-1} also for SA, and 2930 cm^{-1} for the PN/SA salt, further confirms hydrogen bonding interactions in the salt (Fig. 2, Table 1S).[60]

The molecular structure of SA, as observed in the FTIR spectrum, reveals strong, broad bands in the 1200 – 1000 cm^{-1} range due to ν(C–O), ν(C–C), and in-plane β(C–H) vibrations. The in-plane C–H vibrations also extend over a broader range of 1450 – 1000 cm^{-1}, while strong out-of-plane C–H motions in aromatic compounds are observed in the 1000 – 750 cm^{-1} range (Figure 2, Table 1S). In the narrow range of 1420 – 1300 cm^{-1}, β(O–H) in-

plane deformations, coupled with C–H bending and ring-stretching vibrations, appear as very broad bands. Additionally, the region between 710 – 520 cm^{-1} is generally associated with out-of-plane bending vibrations of the O–H group, characteristic of alcohols and phenols.[61,62]

The FTIR spectrum of SA is characterized by narrow, medium-intensity bands in the 1456 – 1317 cm^{-1} range, primarily attributed to in-plane deformations associated with the presence of methyl groups in its structure. Additionally, a band at 1692 cm^{-1}, occurring as a strong band in the spectra of SA and a weak band in the PN/SA physical mixture, is related to ν(C=O) vibrations. This band is absent in the FTIR spectrum of the PN/SA salt, indicating that deprotonation of the carboxyl group has occurred (Fig. 2). As a result, charge delocalization across the carboxylate anion (toward O4 and O5) forms two hydrogen bonds with the PN molecule from tetrameric rings A and B in the crystal structure of this salt.[34]

Comparing the Raman stretching vibrations related to the aromatic rings, in the 1650 – 1200 cm^{-1} range, we see a ring stretching band at 1614 cm^{-1} with a shoulder at 1593 cm^{-1}, and banding/scissoring δ(C–OH) and δ(CH3) vibrations at 1515 cm^{-1} and 1455 cm^{-1}, respectively, appear in the FTIR spectra of both SA and the PN/SA physical mixture as strong and weak bands. Moreover, the PN/SA salt exhibits a strong band at 1565 cm^{-1}, along with slightly shifted weak bands at lower wavenumbers, 1513 cm^{-1} and 1464 cm^{-1} (Fig. 2 and Fig. 4, Tables 1S, 2S).

Strong FTIR bands in the 1260 – 1000 cm^{-1} region correspond to ν(C–O) stretching vibrations, which are also coupled with the adjacent ν(C–C) vibrations. A doublet band at 1194 /1173 cm^{-1} and at 1101 cm^{-1}, strong for SA and weak for the PN/SA physical mixture, are observed in this region. In contrast, in the FTIR spectrum of the PN/SA salt, the former bands are intense and shifted to 1198 cm^{-1}, being accompanied by very weak shoulders at 1213 cm^{-1} and 1181 cm^{-1}, as well as a strong doublet at 1112/1097 cm^{-1}.

The FTIR band at 767 cm^{-1} and the doublet at 685/668 cm^{-1} in the SA and PN/SA physical mixture spectra are shifted to 786 cm^{-1} and to 674 cm^{-1} in the spectrum of the PN/SA salt. These bands correspond to out-of-plane bending and twisting deformations of the O–H group.

The Raman spectrum of SA shows bands due to C–H stretching vibrations at 2856/2833 cm^{-1} (doublet), 2973 cm^{-1}, and 2943 cm^{-1}. These bands are absent in the Raman spectra of the PN/SA salt.

Two weak Raman bands related to aromatic C–H modes in SA, at 3096 cm^{-1} with a shoulder at 3083 cm^{-1}, are shifted in the spectrum of the PN/SA salt to a medium-intensity doublet 3083/3080 cm^{-1}, accompanied by an additional very weak band at 3065 cm^{-1}. The most intense ν(C–H) band at 3034 cm^{-1} (SA) does not appear in the PN/SA salt spectrum, where the strongest band is shifted to a lower wavenumber (2929 cm^{-1}) and accompanied by medium-intensity bands at 3029 cm^{-1} and 3002 cm^{-1} (Table 2S). This band in the FTIR spectra of SA and the PN/SA physical mixture is seen at 3028 cm^{-1} but is shifted to a lower wavenumber (3000 cm^{-1}) as a medium-intensity signal in the PN/SA salt.

Moreover, two broad peaks at 3357 cm^{-1} and 3216 cm^{-1} in SA and PN/SA physical mixture, attributed to the stretching ν(O–H) mode from the carboxylic group (COOH) and phenol moiety, diminish in the spectrum of the PN/SA salt. This indicates that carboxylic and phenol groups participate in salt formation with PN molecules through hydrogen bonding interactions (Fig. 4, Table 2S).

The strong band at 1698 cm^{-1} in the Raman spectrum of SA, assigned to ν(C=O), is absent in the corresponding spectrum of the PN/SA salt (Fig. 4, Table 2S).

3.2.2.1. *C–H vibrations*

The C–H stretching vibrations in the range of 3100 – 3000 cm^{-1} are a typical spectral fingerprint for aromatic compounds.[64] Two weak bands assigned to aromatic C–H modes in the Raman spectra of SA, observed at 3096 cm^{-1} with a shoulder at 3083 cm^{-1}, are shifted to a medium-intensity doublet at 3083/3080 cm^{-1} and an additional very weak band at 3065 cm^{-1} in the spectra of the PN/SA salt. The most intense aromatic ν(C–H) band found at 3034 cm^{-1} in the Raman spectra for SA is largely suppressed in the PN/SA salt, where the strongest band from C–H stretching vibrations occurs at 2929 cm^{-1}, accompanied by medium-intensity aromatic ν(C–H) bands at 3002 and 3029 cm^{-1} (Fig. 4, Table 2S).

In substituted benzenes, in-plane C–H bending vibrations occur in the frequency range of 1300 – 1000 cm^{-1}, while out-of-plane bending vibrations appear in the frequency range of 1000 – 750 cm^{-1}.[65,66]

3.2.2.2. *Benzene/aromatic ring vibrations*

The C–C stretching ring vibrations are expected to appear in the region from 1600 cm^{-1} to 1585 cm^{-1}. Additionally, the C–C stretching vibrations of the ring is also expected to appear between 1500 cm^{-1} and 1400 cm^{-1}. The stretching vibrations related to the aromatic rings in the SA and PN/SA physical mixture appear in the Raman spectra in the 1650 – 1200 cm^{-1} range, whereas the ring stretching band at 1614 cm^{-1}, and its shoulder at 1593 cm^{-1} appear in their corresponding FTIR spectra as strong and weak bands, respectively.

On the other hand, the PN/SA salt exhibits a medium band at 1565 cm^{-1}, as well as slightly shifted weak bands at lower wavenumbers of 1513 cm^{-1} and 1464 cm^{-1} (Table 1S). The ring-stretching mode is evidenced by a strong band in the Raman spectra of both SA and PN/SA salt at 1591 cm^{-1}. The weak bands in the SA at 1515 cm^{-1}, 1466 cm^{-1}, 1441 cm^{-1}, 1319 cm^{-1}, and 1258 cm^{-1} shift to weak bands at 1459 cm^{-1} and 1418 cm^{-1}, a medium-intensity band at 1393 cm^{-1}, a strong band at 1347 cm^{-1}, and a medium-intensity band at 1235 cm^{-1} band in the PN/SA salt. Our DFTB calculations predict ring-stretching band appearance at 1530 cm^{-1}.

The C–H Raman bending modes of the methyl groups and the aromatic C–C–H deformations[67] in the SA are observed as weak doublet bands at 1183/1177 cm^{-1}, a singlet at 1099 cm^{-1}, and a strong doublet at 1195/1173 cm^{-1} and 1101 cm^{-1}. In the PN/SA salt, these bands are shifted to weak bands at 1111 cm^{-1} and 1049 cm^{-1} (Raman), and to 1111/1098 cm^{-1} and 1048 cm^{-1} (FTIR) (Tables 1S and 2S). Our DFTB calculations predict a band at similar wavenumber of 1074 cm^{-1}.

Vibrational modes with wavenumber below 1000 cm^{-1} have contributions from several internal coordinates related to angle and dihedral angle deformations. Therefore, the strong ν(C–COOH), γ(CH), weak γ(CH) + γ(OH), and γ(OH) modes at 935 cm^{-1}, 801 cm^{-1}, 735 cm^{-1}, and 691 cm^{-1}, respectively, as a Raman fingerprint for SA, are shifted to medium-intensity bands at 912 cm^{-1}, strong bands at 806 cm^{-1} and 739, and medium bands 687 cm^{-1} in the spectrum of the PN/SA salt (Table 2S). These modes also appear in the FTIR spectrum of SA as strong bands at 1018/994 cm^{-1}, 766 cm^{-1}, and 685/688 cm^{-1}, which are shifted to bands of the same intensity at 742 cm^{-1}, but weaker at 674 cm^{-1} in the PN/SA salt (Table 1S).

Additionally, out-of-plane ring bending, γ(ring), assigned as bands at 582 cm^{-1}, 541 cm^{-1}, 478 cm^{-1} (weak), as well as out-of-plane-bending γ(C–C–C) at 296 cm^{-1} in the Raman spectrum of SA, emerge in the spectrum of the PN/SA at 585 cm^{-1}, a doublet at 541/536 cm^{-1}, and additional bands at 509 cm^{-1}, 495 cm^{-1}, and 408 cm^{-1} for γ(ring), and at 159 cm^{-1} for γ(C–C–C). The broad torsional vibration mode for the PN/SA salt

appears at 574 cm⁻¹ in the Raman spectrum and at 575 cm⁻¹ in the FTIR spectrum (Table 1S and 2S). According to our DFTB predictions, the ring breathing mode is expected to appear at 910 cm⁻¹, while ring torsions are predicted at 595 cm⁻¹, 540 cm⁻¹, 897 cm⁻¹, and 912 cm⁻¹.

3.2.2.3. *CH₃ vibrations*

The stretching CH_3 modes characteristic of Raman in the 3050 – 2900 cm⁻¹ range for SA, attributed to the two methoxy groups (O–CH₃), appear as a doublet at 2856/2833 cm⁻¹ and at 2973 cm⁻¹ and 2943 cm⁻¹ for symmetric and asymmetric stretching, respectively. These bands are absent in the Raman spectra of the PN/SA salt (Table 2S). Two weak Raman bands related to aromatic C–H modes in SA, observed at 3096 cm⁻¹ with a shoulder at 3083 cm⁻¹, are shifted to a medium-intensity doublet at 3083/3080 cm⁻¹, with an additional very weak band at 3065 cm⁻¹ in the spectrum of the PN/SA salt. The two medium-intensity asymmetric stretching modes in the Raman spectra at 2972 cm⁻¹ and 3029 cm⁻¹, as well as the symmetric mode at 3040 cm⁻¹ in the SA spectrum are shifted to 2969 cm⁻¹, 2999 cm⁻¹, and 2930 cm⁻¹ in the corresponding spectrum of the PN/SA salt, respectively (Table 2S)1.

The FTIR spectrum of SA is characterized by narrow, medium-intensity bands in the range of 1456 – 1317 cm⁻¹, attributed mainly to in-plane deformations associated with the presence of methyl groups in its structure (Table 1S). The out-of-plane bending mode of H–C–H in CH₃ group is assigned to the strong band at 1455 cm⁻¹, which shifts to a medium-intensity band at 1465 cm⁻¹ in the FTIR spectrum. DFTB calculations predict similar general trends, with in-plane deformations appearing at 1483 cm⁻¹ and 1425 cm⁻¹, and stretching vibrations at 3072 cm⁻¹, 3034 cm⁻¹, 1487 cm⁻¹, and 1439 cm⁻¹.

3.2.2.4. *C=O vibrations*

The C=O stretching vibrations affect the dipole moment, resulting in a prominent peak in the FTIR spectra in the region of 1750 – 1650 cm⁻¹.[68] An intramolecular charge transfer from the donor to acceptor group through a conjugated single-double bond pathway causes changes in the dipole moment and molecular polarizability, which, in turn, influence the FTIR and Raman characteristics. The C=O stretching mode is evidenced by the high values of computed FTIR intensity and Raman activity, which shows simultaneous activation of both FTIR and Raman modes, and reflects the charge transfer

interaction between the donor and acceptor via the conjugated path. Our DFTB calculations support these observations, with the C=O stretching band centroid predicted to appear at 1687 cm⁻¹.

A strong band at 1692 cm⁻¹ in the SA spectrum, with weak intensity in the PN/SA physical mixture, is associated with ν(C=O) vibrations. This band vanishes in the FTIR spectrum of the PN/SA salt (Figure 2), indicating complete deprotonation of the carboxyl group. Consequently, charge delocalization across the carboxylate anion (toward O4 and O5) forms two hydrogen bonds with the PN molecule, resulting in tetrameric rings A and B in the crystal structure of this salt.[34] The absence of the 1696 cm⁻¹ band in the Raman spectrum of the PN/SA salt (Fig. 4, Table 2S), while it is present in the surface enhanced Raman spectrum (SERS) of SA[63], confirms the deprotonation of carboxylic group and the presence of a carboxylate counterion in the structure of the PN/SA salt. Additionally, the strong and weak bands at 1591 cm⁻¹ in the Raman and FTIR spectra of SA, as well as the strong (Raman) and weak (FTIR) band at 1392 cm⁻¹ in PN/SA, confirms the existence of the carboxylate symmetric mode due to charge delocalization (Tables 1S and 2S, Fig. 2).

In general, strong bands in the 1260 – 1000 cm⁻¹ region correspond to ν(C–O) stretching vibrations, which are also coupled with the adjacent ν(C–C) vibrations in the FTIR spectra. In this range, a doublet band at 1194/1173 cm⁻¹ and 1101 cm⁻¹ is strong for SA and weak for the PN/SA physical mixture, respectively. In the FTIR spectrum of the PN/SA salt, these signals are recorded as intense bands shifted to 1198 cm⁻¹, accompanied by very weak shoulders at 1213 cm⁻¹ and 1181 cm⁻¹, as well as a strong doublet band at 1112/1097 cm⁻¹ (Table 1S).

Very intense bands at 767 cm⁻¹ and a doublet at 685/668 cm⁻¹ in the Raman spectrum of SA, which appear as weak bands in the PN/SA physical mixture, are shifted, resulting in an intense maximum at 786 cm⁻¹ and weak counterpart at 674 cm⁻¹ in the corresponding FTIR spectrum of the PN/SA salt. These bands are assigned to the out-of-plane bending vibrations of the O–H group.

The strong band at 1698 cm⁻¹ in the Raman spectrum of SA, assigned to ν(C=O) is not observed in the corresponding spectrum of the PN/SA salt (Figure 4). However, the strong band at 1591 cm⁻¹, related to ring stretching and bending of C–H and C–O, appears in both spectra of the compounds. This suggests that SA molecules do not form dimers and exist in their carboxylate form in the PN/SA salt (Table 2S).[60,63]

Very intense bands at 767 cm^{-1} and a doublet at 685/668 cm^{-1} in the FTIR spectra of SA (weak in the PN/SA physical mixture) are shifted to 786 cm^{-1} and 674 cm^{-1} in the PN/SA salt, and are attributed to out-of-plane O–H bending vibrations (Fig. 2).

For the PN/SA salt, the computed C–H bond length is 1.079 – 1.095 Å, while the experimental value ranges from 0.930 – 0.961 Å. The carboxylate C=O distance is 1.213 Å and C–O distance is 1.325 Å by experiment, with the corresponding calculated values being 1.212 Å and 1.362 Å, respectively. The O–H distance is observed as 0.820 Å and calculated as 0.968 Å by DFT, indicating that the two O–H bonds in syringic acid are involved in intermolecular hydrogen bonding, stabilizing the structure. The O7–C13 distance is 1.362 Å/1.368 Å, as confirmed by DFT calculations and experiment, respectively. Similarly, the O8–C12 distance is 1.372 Å/1.359 Å, as observed by the DFT method and experiment, respectively.[69] For syringic acid, the C–C–C bond angles of the benzene ring range from 118.94° and 120.77°, which closely match the DFT results of 119.4° to 120.9°. The carboxylate angle O4–C9–O5 calculated by DFT is 121.40°, while the experimental value is 122.47°. The tetrahedral angle O–CH$_3$ in the salt structure is 109.5°, which agrees closely with the experimental value.[34] The dihedral angle shows that the entire syringic acid molecule is planar,[34] with a small deviation observed by 2.6°, from the adjacent PN molecule (Fig. 1a).

3.2.3. *Ferulic acid and PN/FA·H$_2$O salt*

The wavenumbers, intensities, and band assignments occurring in the FTIR and Raman spectra of ferulic acid and the studied PN/FA·H$_2$O salt are provided in Tables 1S and 2S and illustrated in Figures 3 and 4.

3.2.3.1. *O–H vibrations*

The band assigned to the ν(OH)$_{Ar}$ stretching vibrations of the substituent on the ring in the FTIR spectrum of FA appears at 3437 cm^{-1}, while it is registered at 3459 cm^{-1} in the spectrum of the PN/FA·H$_2$O salt (Figure 3). This obvious band shift indicates hydrogen bond interactions with the cocrystallized water molecules that interact with the layers in the crystal structure of the salt.[34] The hydrogen bonding effect through the hydroxyl group also leads to a dimer conformation, with the OH stretching mode calculated at 3283 cm^{-1}, which is much closer to the FTIR experimental observation at 3437 cm^{-1} for FA (Fig. 3, Table 1S).

The high polarity of this functional group (O6–H) influences the stretching vibrational mode in the Raman spectrum of FA at 3437 cm^{-1} (very weak), which is absent in the corresponding spectrum of the PN/FA·H$_2$O salt (Fig. 4 and Table 2S).

The O–H in-plane bending vibrations in phenols is a characteristic mode that occurs in the 1250 – 1150 cm^{-1} region. This mode is less sensitive due to the weak hydrogen bonding of the hydroxyl group compared to its stretching and out-of-plane bending modes.[70] The weak band assigned to the O6–H in-plane bending vibration in the FTIR spectrum of FA at 1155 cm^{-1} is shifted to a strong signal at 1131 cm^{-1} for the PN/FA·H$_2$O salt. A medium-intensity band assigned to the O–H out-of-plane bending vibration observed in the FTIR spectrum of FA at 597 cm^{-1}, is shifted to a very strong signal at 574 cm^{-1} in the PN/FA·H$_2$O spectrum (Fig. 3, Table 1S).

3.2.3.2. *C–H vibrations*

The aromatic moieties are detected in the vibrational spectra due to the bands from C–H stretching vibrations in the region of 3100 – 3000 cm^{-1}.[59] The FTIR band from C–H stretching of the benzene ring for FA and PN/FA·H$_2$O salt is registered at 3077 cm^{-1} and 3000 cm^{-1}, respectively (Table 1S). This observed position is also in agreement with the weak Raman band at 3061 cm^{-1} for FA, though it is absent in the corresponding spectrum of PN/FA·H$_2$O (Figure 4). In line with the FTIR experimental data, DFTB predicts bands at 3120 cm^{-1}, 3034 cm^{-1}, and 3028 cm^{-1}.

The aromatic C–H in-plane bending modes of benzene and its derivatives are typical vibrations seen as sharp, weak to medium intensity bands in the 1300 – 1000 cm^{-1} region. In the Raman spectrum of FA, C–H in-plane bending vibrations appear at 1312 cm^{-1}, 1270 cm^{-1}, and 1175 cm^{-1}, which shifted to 1319 cm^{-1}, 1270 cm^{-1}, 1263 cm^{-1}, and 1193/1162 cm^{-1} in the PN/FA·H$_2$O salt spectrum. The medium to strong intensity FTIR bands in FA at 1461 cm^{-1}, 1375 cm^{-1}, 1265 cm^{-1}, and 1200 cm^{-1} appear at 1424 cm^{-1} (weak), 1321 cm^{-1} (strong), and 1269 cm^{-1} (strong) in the corresponding spectrum of the PN/FA·H$_2$O salt.

The Raman weak to medium intensity out-of-plane bending vibrations in the 980 – 850 cm^{-1} region of FA appear with same intensities at 974 and 880 cm^{-1} in the spectrum of the PN/FA·H$_2$O salt. This vibrational mode agrees with the associated strong bands at 969 cm^{-1} and at 847 cm^{-1} in the FTIR spectrum of FA and at 974 cm^{-1} and 846 cm^{-1} in the PN/FA·H$_2$O salt.

3.2.3.3. *COOH vibrations*

A single band observed in the 1800 – 1700 cm^{-1} range corresponds to C=O stretching vibrations. The nature of the carbonyl group arises from the presence of a lone pair of electrons on the more electronegative oxygen atom, along with the delocalization of bound electrons toward the less electronegative carbon atom, leading to the formation of the double bond.[71] The carbonyl group, as part of a carboxylic acid, influences hydrogen bonding between carboxylic groups, potentially leading to dimer formation in the solid state.

Two weak FTIR bands observed at 1821 cm^{-1} and 1733 cm^{-1} in the spectra of FA and the PN/FA·H$_2$O physical mixture are assigned to C=O stretching vibrations, and is characteristic of the neutral form of the carboxylic acid, acting as a coformer in the synthesis of the PN/FA·H$_2$O salt (Fig. 3).

The very strong stretching mode of the carbonyl group ν(C=O) at 1686/1660 cm^{-1}, along with the in-plane deformation of the hydroxyl group within the carboxylic group at 1429/1407 cm^{-1}, are observed in the FTIR spectrum of FA. The former band shifts to 1661 cm^{-1}, while the latter is not evident in the corresponding spectrum of the PN/FA·H$_2$O salt (Fig. 3, Table 1S). However, the strong FTIR doublet for the ν(C=O) mode at 1686/1660 cm^{-1} in the FA spectrum and its absence in the PN/FA·H$_2$O salt spectrum indicate the deprotonation of the carboxylic group (Fig. 3, Table 1S). This deprotonation leads to electron delocalization in the carboxylate anion, forming hydrogen bonds toward the O5 atom, by interacting with both the N1 atom of the pyridoxonium cation and the O1 atom of a water molecule (Fig. 1b).

Depending on whether FA exists as a monomeric form or as hydrogen-bonded dimers in the solid state, C–O stretching and C–O bending vibrations for carboxylic acids typically occur in the 1350 – 1200 cm^{-1} and 750 – 650 cm^{-1} regions, respectively. However, aromatic and aliphatic chain vibrations in the molecular structure of FA and PN/FA·H$_2$O salt overlap with these C–O vibrations, making assignments complex and ambiguous. Additionally, the strong band at 1201 cm^{-1} in the FTIR spectra of FA and the PN/FA·H$_2$O physical mixture is represented by a weak band at 1223 cm^{-1} in the PN/FA·H$_2$O salt, confirming the presence of carboxylate anions that participate in hydrogen bonding within the salt structure (Fig. 3, Table 1S).

In the Raman spectrum of FA, the bands at 233 cm^{-1} and 157 cm^{-1} are assigned to the C– COOH in-plane and out-of-plane bending vibrations, respectively, and are in agreement with both the literature and our DFTB calculations (258 cm^{-1} and 193 cm^{-1}).[72] However, these two bands shift in the spectrum of PN/FA·H$_2$O, with the former splitting into two weak bands at 253/246 cm^{-1} (doublet) and 227 cm^{-1}, and the latter appearing as a medium-intensity shoulder band at 159(w)/150(m) cm^{-1} (Figure 4, Table 2S).

3.2.3.4. *O–CH$_3$ group vibrations*

The stretching O–CH$_3$ mode in FA is observed as a very strong FTIR band at 1030 cm^{-1}, while its intensity is significantly reduced in the spectrum of the PN/FA·H$_2$O salt. DFTB calculations predict this band to appear at 1063 cm^{-1}. Although the C–O–CH$_3$ angle bending mode for *m*-methoxy benzaldehydes overlaps with the ring planar C–C–C angle bending modes in the region of 300 – 670 cm^{-1}, in the Raman spectrum of FA,[73,74] this mode is observed as a strong band at 335 cm^{-1} but is absent in the spectrum of the PN/FA·H$_2$O salt. The torsional mode of the O–CH$_3$ group in anisole was observed at 100 cm^{-1}.[75] In the Raman spectrum of the PN/FA·H$_2$O salt, it is observed as a strong band at 98 cm^{-1} (Table 2S). The calculated frequency for this mode at 87 – 76 cm^{-1}, using the B3LYP/6-31G(d,p) method (mode nos. 63 and 64), is in very good agreement with the experimental value. Our current DFTB calculations give slightly higher values for this mode, around 98 cm^{-1}.

3.2.3.5. *CH$_3$ vibrations*

The methyl hydrogen atoms in the electron density potential (EDP) are simultaneously subjected to hyperconjugation and backdonation, leading to a decrease in stretching wavenumbers and infrared intensities, as reported in the literature[76] for similar molecular systems. The stretching modes for the O–CH$_3$ and CH$_3$ groups appear in the 2870 – 2825 cm^{-1} and 2953 – 2860 cm^{-1} regions, respectively. Additionally, two asymmetric stretching modes for both groups are observed in nearly the same range 2985 – 2925 cm^{-1}.[76]

The FTIR spectrum of the PN/FA·H$_2$O salt exhibits bands corresponding to the asymmetric and symmetric C–H stretching vibrations of the CH$_3$ group at 2967 cm^{-1} and 2938 cm^{-1}, respectively (Table 1S). Additionally, two weak bands observed at 2984 cm^{-1} and 2943 cm^{-1} are assigned to the C–H asymmetric and symmetric stretching vibrations of the CH$_3$ group, respectively, in agreement with the DFTB predictions at 2990 cm^{-1}, 2983 cm^{-1}, and 2967 cm^{-1}.

The asymmetric CH$_3$ and symmetric CH$_3$ deformation vibrations are observed as a strong band at 1461 cm^{-1} and a weak band at 1463 cm^{-1}, respectively, in the FTIR and Raman spectra of FA. The former exhibits weak intensity at the same wavenumber in the PN/FA·H$_2$O salt, while the latter is absent in its Raman spectrum. The bands corresponding to symmetric CH$_3$ deformations, occurring at 1375 cm^{-1} and 1374 cm^{-1} for FA, shift to 1377 cm^{-1} and 1380 cm^{-1} for the PN/FA·H$_2$O salt in the FTIR and Raman spectra, respectively (Fig. 3 and Fig. 4). Additionally, the CH$_3$ torsional mode is observed as a strong band at 157 cm^{-1} in the Raman spectra of FA, emerging as a medium-intensity band at 150 cm^{-1} in the PN/FA·H$_2$O salt (Fig. 4, Table 2S).

3.2.3.6. *Benzene/aromatic ring vibrations*

Six equal C–C bonds in the benzene and three C–C bonds in the substituent chain contribute to nine C–C stretching vibrational modes. Moreover, the in-plane and out-of-plane bending vibrations of the C–C–C ring contribute to the fingerprint region, though many of these modes are inactive in the IR wavelength range due to the high symmetry of the benzene ring. Skeletal stretching C–C bands for benzene derivatives typically appear around 1650 – 1400 cm^{-1}.[67]

The deformation of the phenyl ring's C–C–C angles give rise to bands at 1030 cm^{-1}, 910 cm^{-1}, 750 cm^{-1}, 684 cm^{-1}, and 597 cm^{-1} in the FTIR spectrum of FA and at 749/741 cm^{-1} and 670 cm^{-1} in the Raman spectra (Fig. 3 and Fig. 4, Tables 1S and 2S), as compared to DFTB predictions at 1064 cm^{-1}, 948 cm^{-1}, 824 cm^{-1}, 732 cm^{-1}, 678 cm^{-1}, and 735 cm^{-1}.

The stretching vibrations of the C–C bonds in the aromatic ring and the substituted chain in FA, appearing at 1588 cm^{-1} and 1617 cm^{-1}, shift to a strong band at 1547 cm^{-1}, with a shoulder at 1525 cm^{-1} in the FTIR spectrum of the PN/FA·H$_2$O salt. The corresponding DFTB predictions are at 1612 cm^{-1} and 1548 cm^{-1}.

3.3. *Thermal analyses*

The TG/DTG and DSC curves of PN/SA in Figure 5 confirm the anhydrous nature of the salt. Specifically, the DSC curve (Fig. 5c) shows a single melting endotherm (T_{onset} = 130.0 °C and T_{peak} = 132.5 °C), while the TG curve (Fig. 5a) exhibits a mass loss of only 0.34 % up to 110 °C, which is typical for anhydrous substances. The melting of the salt is followed by thermal decomposition, evident in the TG curve as a significant mass loss peaking around 200 °C, as shown in the DTG curve (Fig. 5b).
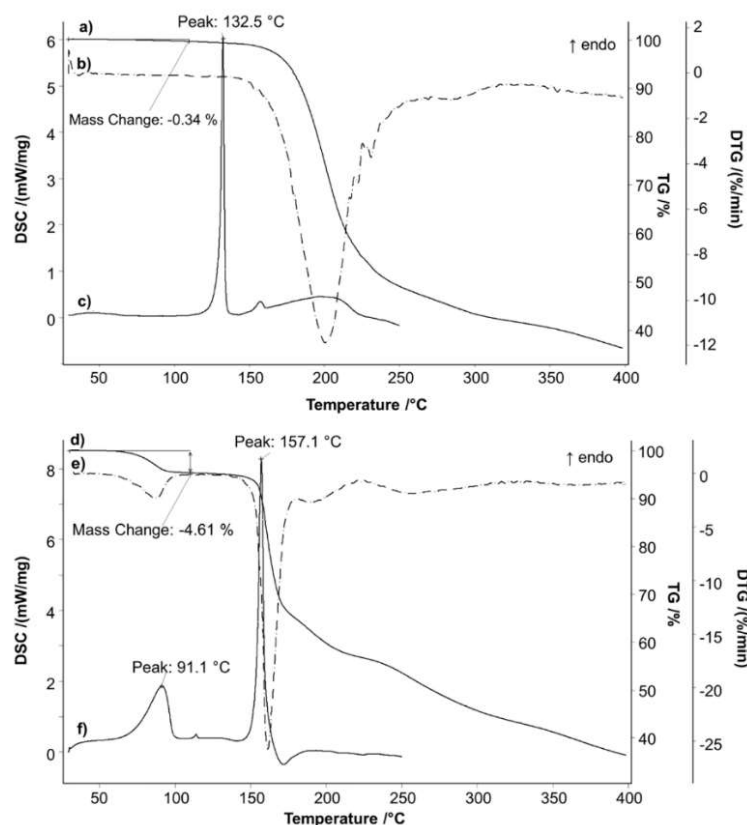

Fig. 5. TG (**a**), DTG (**b**), and DSC (**c**) curves of PN/SA salt and TG (**d**), DTG (**e**), and DSC (**f**) curves of PN/FA·H$_2$O salt

The TG/DTG and DSC curves of PN/FA·H$_2$O are also presented in Figure 5. The DSC curve (Fig. 5f) shows an asymmetric endotherm (T_{onset} = 73.5 °C and T_{peak} = 91.1 °C), which is attributed to the evaporation of one water molecule from the salt structure. This is followed by the melting of the anhydrous cocrystal, characterized by a sharp endotherm (T_{onset} = 153.8 °C and T_{peak} = 157.1 °C). The TG curve (Figure 5d) shows a mass loss of 4.61 % up to 110 °C, which closely matches the theoretically calculated mass fraction of 4.72 % for one water molecule in the structure of PN/FA·H$_2$O. The monohydrate salt melts and decomposes, as indicated by a significant mass loss on the TG curve (with the maximum rate around 160 °C, Fig. 5e), which coincides approximately with the melting temperature of the salt.

4. CONCLUSIONS

The FTIR spectra of the PN/SA and PN/FA·H$_2$O salts reveal the appearance of modes related to carboxylate anion vibrations, specifically asymmetric and symmetric stretching vibrations at 1567 cm^{-1} and 1550 cm^{-1} and 1390 cm^{-1} and 1377 cm^{-1}, respectively. These bands are absent in the corresponding spectra of the SA and FA coformers.[77] Differences between the FTIR and Raman spectra of the starting deprotonated pyridoxine base (PN) and the obtained PN/SA and PN/FA·H$_2$O salts are also observed in the deformation mode regions at 992 cm^{-1} (PN/SA) and 974 cm^{-1} (PN/FA·H$_2$O), which do not appear in the PN spectrum. This finding confirms the presence of the protonated pyridoxonium cation in the salt structures, as also evidenced by the Raman spectra of the salts.

The protonation of the N-atom is marked by a characteristic intense narrow band for the pyridinium cation at 1520 – 1530 cm^{-1}, which is observed in the FTIR spectra[78] of the mechano-chemically synthesized PN/SA and PN/FA·H$_2$O salts at 1515 cm^{-1} and 1532 cm^{-1}, respectively. This band is absent in the FTIR spectrum of PN, further distinguishing the FTIR spectral signature of the salts from that of the neutral PN base. Thermal analysis complements the spectroscopic findings, confirming the authenticity of both mechanochemically synthetized salts.

The thermal profiles of PN/SA and PN/FA·H$_2$O, attributed to the assigned vibrational modes in the spectral fingerprints, confirms the unique solid-state properties of pyridoxine salts with hydroxy derivatives of benzoic acid from natural sources. Further research on the kinetics of PN release *in vitro* and *in vivo* is expected to guide the development of new solid forms of PN as an active pharmaceutical ingredient.

REFERENCES

(1)   Prohotsky, D. L.; Zhao, F., A survey of top 200 drugs-- inconsistent practice of drug strength expression for drugs containing salt forms. *J. Pharm. Sci.* **2012**, *101*(1) 1–6. https://doi.org/10.1002/jps.22735

(2)   Paulekuhn, G. S.; Dressman, J. B.; Saal, C., Trends in active pharmaceutical ingredient salt selection based on analysis of the Orange Book database. *J. Med. Chem.* **2007**, *50*(26), 6665–72. https://doi.org/10.1021/jm701032y

(3)   Morris, K. R.; Fakes, M. G.; Thakur, A. B.; Newman, A. W.; Singh, A. K.; Venit, J. J.; Spagnuolo, C. J.; Serajuddin, A. T. M., An integrated approach to the selection of optimal salt form for a new drug candidate. *Int. J. Pharm.*, **1994**, *105*, 209–217. https://doi.org/10.1016/0378-5173(94)90104-X

(4)   Tong, W-Q; Whitesell, G., In situ salt screening – a useful technique for discovery support and preformulation studies. *Pharm. Dev. Tech.*, **1998**, *3*, 215–223. https://doi.org/10.3109/10837459809028498

(5)   Bastin, J., Bowker, J. M., Slater, J. B. Salt Selection and optimisation procedures for pharmaceutical new chemical entities. *Org. Process Res. Dev* **2000**, *4*(5), 427–435 https://doi.org/10.1021/op000018u

(6)   Sacchetti, M., General equations for in situ salt screening of multibasic drugs in multiprotic acids. *Pharm. Dev. Tech.*, **2000**, *5*, 579–582. https://doi.org/10.1081/PDT-100102042

(7)   Ware, E. C.; Lu, D. R., An automated approach to salt selection for new unique trazodone salts. *Pharm. Res.*, **2004**, *21*, 177–184. https://doi.org/10.1023/B:PHAM.0000012167.60180.c3

(8)   Hammond, R. B.; Hashim, S. R.; Ma, C.; Roberts. J. K., Grid-based molecular modeling for pharmaceutical salt screening: case example of 3,4,5,7,8,9-hexahydro-2H-pyrimido-(1,2-a)-primidinium acetate. *J. Pharm. Sci.* **2006**, *95*(11), 2361–2372. https://doi.org/10.1002/jps.20657

(9)   Black, S. N.; Collier, E. A.; Davey, R. J.; Roberts, R. J., Structure, solubility, screening, and synthesis of molecular salts. *J Pharm Sci.*, **2007**, *96*(5), 1053–68. https://doi.org/10.1002/jps.20927

(10) Elder, D. P.; Delaney, E.; Teasdale, A.; Eyley, S.; Reif, V. D.; Jacq, K.; Facchine, K. L.; Oestrich, R. S.; Sandra, P.; David, F., The utility of sulfonate salts in drug development. *J. Pharm. Sci.*, **2010**, *99*, 2948–2961. https://doi.org/10.1002/jps.22058

(11) Morissette, S. L.; Almarsson, O.; Peterson, M. L.; Remenar, J. F.; Read, M. J.; Lemmo, A. V.; Ellis, S.; Cima, M. J.; Gardner, C. R., High-throughput crystallization: polymorphs, salts, co-crystals and solvates of pharmaceutical solids. *Adv. Drug Deliv. Rev.* **2004**, *56*(3), 275–300. https://doi.org/10.1016/j.addr.2003.10.020

(12) Guerrieri, P.; Rumondor, A. C.; Li, T.; Taylor, L. S., Analysis of relationships between solid-state properties, counterion, and developability of pharmaceutical salts. *AAPS PharmSciTech.* **2010**, *11*(3), 1212–22. https://doi.org/10.1208/s12249-010-9499-4

(13) Gupta, D.; Bhatia, D; Dave, V; Sutariya, V.; Varghese, S. G., Salts of therapeutic agents: chemical, physicochemical, and biological considerations. *Molecules.* **2018**, *23*(7), 1719. https://doi.org/10.3390/molecules23071719

(14) Verbeek, R. K.; Kanfer, I.; Walker, R. B., Generic substitution: the use of medicinal products containing different salts and implications for safety and efficacy. *Eur J Pharm Sci.*, **2006**, *28*, 1–6. https://doi.org/10.1016/j.ejps.2005.12.001

(15) Patel, A.; Jones, S. A.; Ferro, A.; Patel, N., *Pharmaceutical salts: a formulation trick or a clinical conundrum? Br. J. Cardiol* **2009**, *16*, 281–286. https://bjcardio.co.uk/2009/11/pharmaceutical-salts-a-formulation-trick-or-a-clinical-conundrum/

(16) Gilli, P.; Pretto, L.; Bertolasi, V.; Gilli, G., Predicting hydrogen-bond strengths from acid−base molecular properties. The pK_a slide rule: toward the solution of a long-lasting problem. *Acc. Chem. Res.* **2009**, 42, 33–44. https://doi.org/10.1021/jp904812b

(17) Gilli, P.; Gilli, G., Hydrogen bond models and theories: The dual hydrogen bond model and its consequences. *J. Mol. Struct.* **2010**, *972*, 2–10. https://doi.org/10.1016/j.molstruc.2010.01.073

(18) Cruz-Cabeza, J. A., Acid–base crystalline complexes and the pKa rule. *CrystEngComm 2012, 14,* 6362–6365. https://doi.org/10.1039/C2CE26055G

(19) Nangia, A., Supramolecular chemistry and crystal engineering. *J. Chem. Sci.* **2010**, *122*(3), 295–310. https://doi.org/10.1007/s12039-010-0035-6

(20) Almarsson, O.; Zaworotko, M. J., Crystal engineering of the composition of pharmaceutical phases. Do pharmaceutical co-crystals represent a new path to improved medicines? *Chem. Commun.* **2004**, *7*(17), 1889–96. https://doi.org/10.1039/B402150A

(21) Elder, D. P.; Holm, R.; De Diego H. L., Use of pharmaceutical salts and cocrystals to address the issue of poor solubility. *Int. J. Pharm.* **2012**, *453*, 88–100. https://doi.org/10.1016/j.ijpharm.2012.11.028

(22) Berry, J. D.; Steed, W. J., Pharmaceutical cocrystals, salts and multicomponent systems, intermolecular interactions and property based design, *Adv. Drug Deliv. Rev* **2017**, *1*(117), 3–24. https://doi.org/10.1016/j.addr.2017.03.003

(23) Desiraju, R. G., Crystal engineering: from molecule to crystal. *J. Am. Chem. Soc.* **2013**, *135*(27), 9952–9967 https://doi.org/10.1021/ja403264c

(24) Childs, L. S.; Patrick G. S.; Park, A., The salt−cocrystal continuum: the influence of crystal structure on ionization state, *Mol. Pharmaceutics* **2007**, *4*(3), 323–338. https://doi.org/10.1021/mp0601345

(25) Aakeröy, C. B.; Fasulo, M. E.; Desper, J., Cocrystal or salt: does it really matter? *Mol. Pharmaceutics* **2007**, *4*(3), 317–22. https://doi:10.1021/mp060126o

(26) Aitipamula, S. *et al.,* Polymorphs, salts, and cocrystals: what's in a name? *Cryst. Growth Des.* **2012**, *12*(5), 2147–2152. https://doi.org/10.1021/cg3002948

(27) Haynes, D. A.; Jones, W.; Motherwell, W. D. S., Occurrence of pharmaceutically acceptable anions and cations in the Cambridge structural database. *J. Pharm. Sci.* **2005**, *94(10)*, 2111–2120. https://doi.org/10.1002/jps.20441

(28) Grothe, E.; Meekes, H.; Vlieg, E.; Ter Horst, J. H.; De Gelder R., Solvates, salts, and cocrystals: a proposal for a feasible classification system, *Cryst. Growth Des.* **2016,** *16*(6), 3237–3243. https://DOI:10.1021/acs.cgd.6b00200

(29) Ranjit, T.; Sarma, B., Drug-drug and drug-nutraceutical cocrystal/salt as alternative medicine for combination therapy: a crystal engineering approach. *Crystals* **2018**, *8*(2), 101. https://doi.org/10.3390/cryst8020101

(30) Fulas, O. A; Laferrière, A.; Ayoub, G.; Gandrath, D.; Mottillo, C.; Titi, H. M.; Stein, R. S.; Friščić, T.; Coderre, T. J., Drug-nutraceutical co-crystal and salts for making new and improved bi-functional analgesics. *Pharmaceutics* **2020**, *12*, 1144. https://doi.org/10.3390/pharmaceutics12121144

(31) Jin, S.; Haskins, M. M.; Deng, C.-H.; Matos C. R. M. O.; Zaworotko, J. M., Crystal engineering of ionic co-crystals comprising Na/K salts of hesperetin with hesperetin molecules and solubility modulation. *IUCrJ* **2023**, *10,* 329–340. https://doi:10.1107/S205225252300266X

(32) Hasa, D.; Perissutti, B.; Cepek, C.; Bhardwaj, S.; Carlino, E.; Grassi, M.; Invernizzi, S.; Voinovich, D., Drug salt formation via mechanochemistry: the case study of vincamine *Mol. Pharmaceutics* **2013**, *10*(1), 211–224. https://dx.doi.org/10.1021/mp300371f.

(33) Solares-Briones, M.; Coyote-Dotor, G.; Páez-Franco, J. C.; Zermeño-Ortega, M. R.; De la O Contreras, C. M.; Canseco-González, D., Avila-Sorrosa, A, Morales-Morales, D.; Germán-Acacio, J. M., Mechanochemistry: a green approach in the preparation of pharmaceutical cocrystals. *Pharmaceutics* **2021**, *25, 13*(6):790. https://doi.org/10.3390/pharmaceutics13060790 \

(34) Cvetkovski, A.; Ferretti, V.; Bertolasi, V., New pharmaceutical salts containing pyridoxine. *Acta Cryst.* **2017**, *C73*, 1064–1070. https://doi.org/10.1107/S2053229617015765

(35) Hayashi, H.; Wada, H.; Yoshimura, T.; Esaki, N.; Soda, K., Recent topics in pyridoxal 5'-phosphate enzyme studies. *An. Rev. Biochem.* **1990**, *59*, 87–110. https://doi:10.1146/annurev.bi.59.070190.000511

(36) Ebadi, M., Regulation and function of pyridoxal phosphate. *CNS Neurochem. Int.* **1981**, *3*(3–4), 181–205. https://doi:10.1016/0197-0186(81)90001-2

(37) Seiler, D.; Doser, K.; Salem, I., Relative bioavailability of prasugrel free base in comparison to prasugrel hydrochloride in the presence and in the absence of a proton pump inhibitor. *Arzneimittelforschung* **2011**, *61*, 247–251. https://doi:10.1055/s-0031-1296195

(38) Stahl, P. H.; Skinner, F. S., Pharmaceutical aspects of the API salt form. In: Stahl P. H., Wermuth C. G., (editors). *Pharmaceutical Salts: Properties, Selection, and Use.* 2nd ed. WILEY-VCH, Weinheim, Germany: 2011. pp. 85–124.

(39) Teraoka, R.; Otsuka, M.; Matsuda, Y., Effects of temperature and relative humidity on the solid-state chemical stability of ranitidine hydrochloride. *J. Pharm. Sci.* **1993**, *82* (6), 601–604. https://doi:org/10.1002/jps.2600820611

(40) Thakral, K. N.; Behme, J. R.; Aburub, A.; Peterson, A. J.; Woods, A. T.; Diseroad, A. B.; Suryanarayanan, R.; Stephenson, A. G., Salt disproportion in the solid state: role of solubility and counterion volatility, *Mol. Pharmaceutics* **2016**, *13*(12), 4141–4151. https://DOI:10.1021/acs.molpharmaceut.6b00745

(41) Remenar, F. J; MacPhee, J. M.; Larson, K. B.; Tyagi, A. V.; Ho, H. J.; McIlroy, A. D.; Hickey, B. M.; Shaw, B. P.; Almarsson, Ö., Salt selection and simultaneous polymorphism assessment via high-throughput crystallization: the case of sertraline. *Org. Proc. Res. Dev.* **2003** *7*(6), 990–996 https://DOI:10.1021/op034115

(42) Srinivasulu, C.; Ramgopal, M.; Ramanjaneyulu, G.; Anuradha, C. M.; Kumar C. S., Syringic acid (SA) – a review of its occurrence, biosynthesis, pharmacological and industrial importance. *Biomed.*Pharmacother. **2018**, *108*, 547–557. https://DOI:10.1016/j.biopha.2018.09.069

(43) Ogut, E.; Armagan, K.; Gül, Z., The role of syringic acid as a neuroprotective agent for neurodegenerative disorders and future expectations. *Metab. Brain Dis.* **2022**, *37*(4), 859-880. https://doi:10.1007/s11011-022-00960-3

(44) Srinivasan, M.; Sudheer, R. A.; Menon, P. V.; Ferulic acid: therapeutic potential through its antioxidant property, *J. Clin. Biochem. Nutr* **2007**, *40*(2), 92–100. https://doi.org/10.3164/jcbn.40.92

(45) Chatterjee, N. S.; Anandan, R.; Navitha, M.; Asha, K. K.; Kumar, K. A.; Mathew, S.; Ravishankar, C. N., Development of thiamine and pyridoxine loaded ferulic acid-grafted chitosan microspheres for dietary supplementation. *J. Food Sci. Technol.* **2016** *53*(1), 551–560. https://doi:10.1007/s13197-015-2044-4

(46) Sentkowska, A.; Piwowarczyk, S.; Pyrzyńska, K., Simultaneous determination of vitamin B6 and catechins in dietary supplements by ZIC-HILIC chromatography and their antioxidant interactions. *Eur. Food Res. Technol.* **2020**, *246,* 1609–1615. https://doi.org/10.1007/s00217-020-03516-w

(47) Kaduk, J. A.; Billinge, S. J. L.; Dinnebier, R. E. *et al.,* Powder diffraction. *Nat Rev Methods Primers* **2021,** *1,* 77. https://doi.org/10.1038/s43586-021-00074-7

(48) Elstner, M.; Porezag, D.; Jungnickel, G.; Elsner, J.; Haugk, M.; Frauenheim, Th.; Suhai, S.; Seifert, G., Self-consistent-charge density-functional tight-binding method for simulations of complex materials properties. *Phys. Rev. B* **1998**, *58*, 7260–7268. https://doi.org/10.1103/PhysRevB.58.7260

(49) Gauss, M.; Cui, Q.; Elstner, M., DFTB3: Extension of the self-consistent-charge density-functional tight-binding method (SCC-DFTB). *J. Chem. Theory Comput.* **2011**, *7*, 931–948. https://doi.org/10.1021/ct100684s

(50) Hourahine, B.; Aradi, B.; Blum, V.; Bonafé, F.; Buccheri, A.; Camacho, C.; Cevallos, C.; Deshaye, M. Y.; Dumitrică, T.; Dominguez, A., et al., DFTB+, a software package for efficient approximate density functional theory based atomistic simulations. *J. Chem. Phys.* **2020**, *152*, 124101. https://doi.org/10.1063/1.5143190

(51) Gaus, M.,; Goez, A.,; Elstner, M., Parametrization and benchmark of DFTB3 for organic molecules. *J. Chem. Theory Comput.* **2013**, *9*, 338–354. https://doi.org/10.1021/ct300849w

(52) Gaus, M.; Lu, X.; Elstner, M.; Cui, Q., Parametrization of DFTB3/3OB for sulfur and phosphorus for chemical and biological applications. *J. Chem. Theory Comput.* **2014**, *10*, 1518–1537. https://doi.org/10.1021/ct401002w

(53) Kubillus, M.; Kubar, T.; Gaus, M.; Rezac, J.; Elstner, M., Parametrization of the DFTB3 Method for Br, Ca, Cl, F, I, K and Na in organic and biological systems. *J. Chem. Theory Comput.* **2015**, *11*, 332–342. https://doi.org/10.1021/jp506557r

(54) Monkhorst, H. J.; Pack, J. D.; Special points for brillouin-zone integrations. *Phys. Rev. B* **1976**, *13*, 5188–5192. https://doi.org/10.1103/PhysRevB.13.5188

(55) Šebek, J.; Knaanie, R.; Albee, B.; Potma, O. E; Gerber, R. B., Spectroscopy of the C–H stretching vibrational band in selected organic molecules. *J. Phys. Chem. A* **2013**, *117*(32), 7442–7452. https://doi.org/10.1021/jp4014674

(56) Szafran, M.; Koput J.; Ab initio and DFT calculations of structure and vibrational spectra of pyridine and its isotopomers *J. Mol. Struct.* **2001**, *565–566*, 439–448 https://doi.org/10.1016/S0022-2860(00)00934-0

(57) Srivastava, M.; Rani, P.; Singh, N. P.; Yadav, R. A., Experimental and theoretical studies of vibrational spectrum and molecular structure and related properties of pyridoxine (vitamin B6). *Spectrochim Acta A Mol Biomol Spectrosc.* **2014**, *120*, 274–86. https://doi:10.1016/j.saa.2013.09.133

(58) Cinta, S.; Morari, C.; Vogel, E.; Maniu, D.; Aluas, M.; Iliescu, T.; Cozar, O.; Kiefer, W., Vibrational studies of B6 vitamin. *Vib. Spectrosc.* **1999**, *19, 329–334.* https://doi.org/10.1016/S0924-2031(99)00019-3

(59) Varsányi, G., Assignment for Vibrational Spectra of Seven Hundred Benzene Derivatives, Vol 1. Adam Hilger: London, 1974, pp 280.

(60) Clavijo, R. E.; Ross, D. J.; Aroca, R. F., Surface enhanced Raman scattering of trans-p-coumaric and syringic acids. *J. Raman Spectrosc.* **2009**, *40*, 1984–1988. https://doi.org/10.1002/jrs.2353

(61) Mohammed-Ziegler, I.; Billes, F., Vibrational spectroscopic calculations on pyrogallol and gallic acid. *J. Mol. Struct. Theochem* **2002**, 259–265. https://doi.org/10.1016/S0166-1280(02)00547-X

(62) Selvaraj, S.; Rajkumar, P.; Thirunavukkarasu, K.; Gunasekaran, S.; Kumaresan, S., Vibrational (FT-IR and FT-Raman), electronic (UV–vis) and quantum chemical investigations on pyrogallol: A study on benzenetriol dimers. *Vib. Spectrosc*, **2018**, *95*, 16–22. https://doi.org/10.1016/j.vibspec.2018.01.003

(63) Espina, A.; Sanchez-Cortes, S.; Jurašeková, Z., Vibrational study (Raman, SERS, and IR) of plant gallnut polyphenols related to the fabrication of iron gall inks. *Molecules* **2022**, *27*, 279. https://doi.org/10.3390/molecules27010279

(64) Albo Hay Allah, M., A.; Balakit, A. A.; Salman, H. I.; Abdulridha, A. A.; Sert, Y., New heterocyclic compound as carbon steel corrosion inhibitor in 1 M

H_2SO_4. High efficiency at low concentration: experimental and theoretical studies. *J. Adhesion Sci. Technol.* **2022** *37*(3), 525–547. https://doi.org/10.1080/01694243.2022.2034588

(65) Krishnakumar, V.; Dheivamalar, S., Density functional theory study of fourier transform infrared and raman spectra of 2-amino-5-chloro benzonitrile. *Spectrochim. Acta A Mol. Biomol. Spectrosc.* **2008**, *15,71*(2), 465–70. https://doi:10.1016/j.saa.2007.11.028

(66) Thangarasu, S.; Siva, V.; Asath Bahadur, S.; Athimoolam, S., Structural, vibrational, quantum chemical calculations, thermal and antimicrobial studies on nitrate salt of 3-nitroaniline. *Opt. Quant. Electronics* **2021,** *53*(10), 1–16. https://doi.org/10.1007/s11082-021-03146-w

(67) Jakobsen, R. J.; Bentley, F. F., Vibrational spectra of benzene derivatives. II. Frequency assignments in the CsBr region. *Appl. Spectrosc.* **1964**, *18*(3), 88–92. https://doi:10.1366/000370264789620628

(68) Arjunan, V.; Rani, K.; Santhanalakshmi, T.; Mohan, S. A., Combined experimental and theoretical quantum chemical studies on 4-morpholinecarboxaldehyde. *Spectrochim. Acta. Part A, Mol. Biomol. Spectrosc.* **2011**, *79*(*5*), 1395–401. https://doi.org/10.1016/j.saa.2011.04.074

(69) Sukumaran, S.; Zochedh, A.; Viswanathan, M. T.; Sultan, B. A.; Kathiresan, T., Theoretical investigation of 5-fluorouracil and tamoxifen complex – structural, spectrum, DFT, ADMET and docking simulation. *Polycyclic Aromatic Compounds* **2023**, *43*(*10*), 9443–9460. https://doi.org/10.1080/10406638.2022.2118332

(70) Michalska, D.; Bienko, D. C.; Bienko, A. J. A.; Latajka, Z., Density functional, Hartree−Fock, and MP2 studies on the vibrational spectrum of phenol. *J. Phys. Chem.* **1996**, *100*(45), 17786–17790. https://doi.org/10.1021/jp961376v

(71) Sathyanarayana, D. N., *Vibrational Spectroscopy—Theory and Applications*, Second ed., New Age International (P) Limited Publishers, New Delhi, 2004.

(72) Koczoń, P.; Dobrowolski, J. Cz.; Lewandowski, W.; Mazurek, A. P., Experimental and theoretical IR and Raman spectra of picolinic, nicotinic and isonicotinic acids. *J. Mol. Struct.* **2003**, *655*(1), 89–95 https://doi.org/10.1016/S0022-2860(03)00247-3

(73) Singh, R. N.; Prasad, S. C., Vibrational spectra of isomeric bromoxylenes. *Spectrochim. Acta. A Mol. Biomol. Spectrosc.* **1974**, 34–39. https://doi.org/10.1016/0584-8539(78)80183-4

(74) Sundaraganesan, N.; Kalaichelvan, S.; Meganathan, C.; Joshua, B. D.; Cornard, J., FT-IR, FT-Raman spectra and ab initio HF and DFT calculations of 4-N,N'-dimethylamino pyridine. *Spectrochim. Acta. A Mol. Biomol. Spectrosc.* **2008**, *71*(3), 898–906. https://doi.org/10.1016/j.saa.2008.02.016

(75) Sebastian, S.; Sundaraganesan, N.; Manoharan, S., Molecular structure, spectroscopic studies and first-order molecular hyperpolarizabilities of ferulic acid by density functional study. *Spectrochim. Acta. A Mol. Biomol. Spectrosc.* **2009**, *74*(2), 312–323. https://doi:10.1016/j.saa.2009.06.011

(76) Sajan, D.; Binoy, J.; Hubert Joe, I.; Jayakumar, V. S.; Zaleski, J., Vibrational spectral studies of methyl 3-(4-methoxyphenyl)prop-2-enoate, a new organic non-linear optic crystal. *J. Raman Spectrosc.* **2005**, *36*, 221–236 https://doi.org/10.1002/jrs.1279

(77) Silverstein, R. M.; Webster, F. X.; Kiemle, D. J., *Spectrometric Identification of Organic Compounds*, John Wiley & Sons: Hoboken, NJ, 2005.

(78) Furmanova, N. G.; Verin, I. A.; Shyityeva, N. *et al.,* Synthesis and crystal structure of the coordination compound of pyridoxine with manganese sulfate. *Crystallogr. Rep.* **2011**, *56*, 1033–1037. https://doi.org/10.1134/S1063774511060095